ULTRASONIC IMAGING 3, 113-143 (1981)

EFFECTS OF ANISOTROPY IN THE ULTRASONIC ATTENUATION OF TISSUE ON COMPUTED TOMOGRAPHY[1]

G. H. Brandenburger[2,3], J. R. Klepper[2,4,5], J. B. Miller[4,6], and D. L. Synder[7]

Washington University
St. Louis, MO 63130

We examine the consequences of anisotropy in the ultrasonic attenuation on computed tomography. A phenomenological model for anisotropy in the ultrasonic attenuation of soft, inhomogeneous, tissue-like media is presented. Based upon the model, the effects of anisotropy on transmission tomography are investigated analytically and by computer simulation for simple geometries. Sources of apparent anisotropy in ultrasonic measurements made on intrinsically isotropic media are also discussed. Results of simulations are compared with tomograms of tissue studied in vitro. In particular, reconstruction of a simulated anisotropic heart showed good agreement with the reconstruction of an actual heart.

Introduction

The values exhibited by ultrasonic parameters such as attenuation, speed of sound, and scattering may depend upon the direction of wave propagation and polarization relative to intrinsic directions within the host material. If so, the host material is described as exhibiting anisotropy in the propagation of ultrasound. Although anisotropy in ultrasonic propagation has been well characterized in single crystals (relative to crystalline axes) and in polycrystalline metals (relative to the dominant grain orientation), anisotropic propagation in tissue is incompletely characterized. While reports of anisotropic attenuation date back more than 30 years [1], relatively few systematic studies have been reported [2-5]. The report of Nassiri et al. [5] documents a 2.6 to 1 variation in the ultrasonic attenuation coefficient in skeletal muscle as the direction of progation of longitudinal waves is varied relative to the orientation of the muscle fibers. Variations of similar magnitude were reported from our laboratory in the attenuation coefficient of dog heart [6]. Ultrasonic backscatter from muscle tissue exhibits significant anisotropy [2] and a smaller anisotropy of the velocity of sound in muscle has also been reported

Key words: Anisotropy; attenuation; frequency-dependence; imaging; tissue-characterization; tomography; ultrasound

[1]This work was supported in part by National Institutes of Health Research Grant RR 00396 from the Division of Research Resources and by Research Grant HL 17646 from the Division of Heart and Vascular Diseases, National Heart, Lung and Blood Institute.

[2]Biomedical Computer Laboratory, School of Medicine.

[3]Present address: VARC, Newport News and NASA Langley Research Center, Hampton, Virginia.

[4]Department of Physics.

[5]Present address: Institute of Applied Physiology and Medicine, Seattle, WA 98122.

[6]Address correspondence to J. G. Miller.

[7]Electrical Engineering Department.

0161-7346/81/020113-31$02.00/0

[3]. All of these anisotropies potentially affect any form of ultrasonic imaging where more than one angle of view is used to generate the image.

The purpose of the present study is to examine the consequences of anisotropy in ultrasonic attenuation on computed tomography. We present a phenomenological model for anisotropy of ultrasonic attenuation in soft, inhomogeneous, tissue-like media. The model provides a method for estimating the angular dependence of the ultrasonic attenuation in an irregularly shaped object. The effects of anisotropy on tomographic reconstructions obtained by the use of filtered back projection are examined with the aid of the model. Analytical results are derived for simple object geometries. Numerically generated data are used to demonstrate the consequences of anisotropy on tomographic reconstructions for more complex geometries. Predictions of the consequences of anisotropy are compared with experimentally obtained tomographic reconstructions of the ultrasonic attenuation coefficient of excised dog hearts.

I. A Phenomenological Model of Anisotropy

To investigate the effects of anisotropy on computed tomography, we consider two classes of geometry: linearly-directed anisotropy and tangentially-directed anisotropy. An elemental volume of an anisotropic material is modeled as exhibiting a single direction along which the maximum value of ultrasonic attenuation is measured. This direction is called the anisotropy axis as illustrated in figure 1a, in which anisotropy axes are shown as two-headed arrows to distinguish them from vectors. Anisotropic attenuation is modeled here as identical for propagation directions differing by 180°. A bar and an annulus both exhibiting linearly-directed anisotropy are illustrated in figures 1b and 1c, respectively. The linearly-directed anisotropic bar can be bent into various shapes to illustrate tangentially-directed anisotropy as in the horseshoe and annulus of figures 1d and 1e. In general, more complicated geometries require specification of each differential anisotropic volume element (Fig. 1a) comprising the object. However, a restricted but useful class of object geometries can be modeled by superpositions of macroscopic regions of linearly and tangentially-directed anisotropies.

To examine the effects of anisotropy on computed tomography, we restrict our discussion to the x,y plane. Both the spatial variation of the refractive index, and the magnitude of velocity anisotropy are taken to be small in this model. Consequently, the interrogating ultrasonic energy is assumed to follow the straight-line path from transmitter to receiver. We denote the ultrasonic parameter of interest, usually the ultrasonic attenuation coefficient or its frequency derivative, as $\alpha(x,y,\psi)$. The anisotropic character of this parameter within an area element dxdy is modeled as

$$\alpha(x,y,\psi) = \alpha_o(x,y)(1 + C(x,y,\psi)) \qquad (1)$$

where $\alpha_o(x,y)$ is an intrinsic isotropic component, ψ is the angle between the volume element's anisotropy axis and a fixed coordinate system, and $C(x,y,\psi)$ is the anisotropy angular dependence function, where $C(x,y,\psi) \geq 0$. Vector anisotropy, for which $C(s,y,\psi)$ may be positive or negative, is treated in the discussion section.

An experimental determination of the values of the parameters in Eq. (1) exhibiting only a single anisotropy axis can be carried out if the specimen geometry is known. A simple case is an annulus with a single, linearly-directed, anisotropy axis as in figure 1c. If the interrogating wave is propagated through the center of the annulus, measurements of the parameter

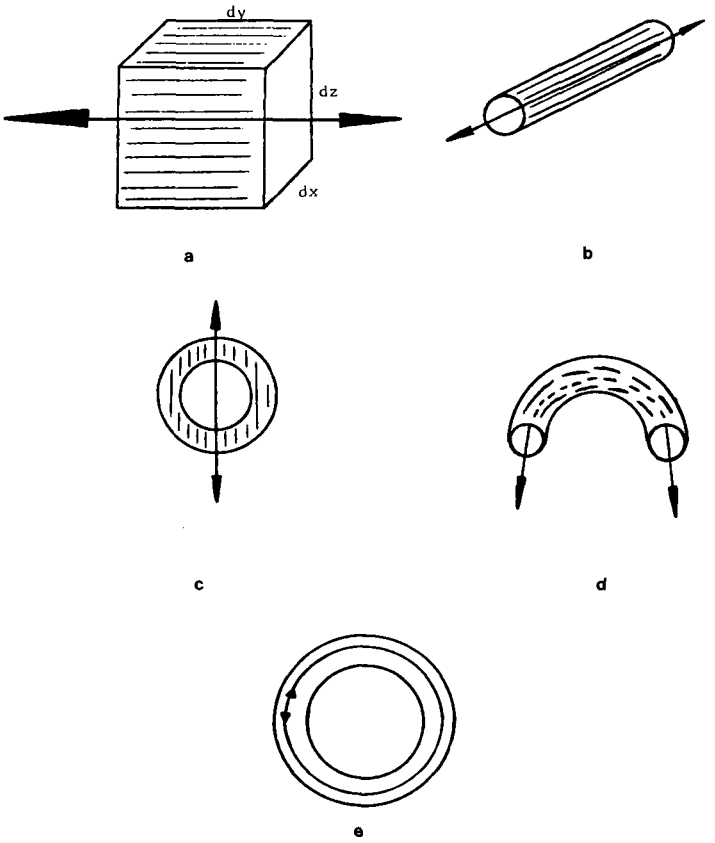

Fig. 1. Four basic geometries of planar anisotropy are illustrated: a) elemental anisotropic volume exhibiting a single linearly-directed axis; b) bar possessing a single linearly-directed anisotropy; c) annulus possessing a single linearly-directed anisotropy; d) example of tangentially-directed anisotropy: the linearly-directed anisotropic bar bent into a half-circle; and e) annulus possessing tangentially-directed anisotropy.

(e.g., slope of the ultrasonic attenuation coefficient versus frequency) made as a function of angle as the disc is rotated yield the anisotropic angle dependence function $C(x,y,\psi)$ directly. Objects not possessing circular symmetry about the rotation axis, such as the bar in figure 1b, require additional knowledge of the object dimensions before the anisotropy can be inferred from simple transmission measurements.

An alternative method for estimating the angular dependence of anisotropy is based on the projection measurements employed in reconstructive tomography. Consider the parallel ray transmission measurements often used in computed tomography. For each view angle, θ, a series of transmission measurements is made over translation positions r, $-a \leq r \leq a$. This set of measurements $p(r,\theta)$ is referred to as the projection line at angle θ,

$$p(r,\theta) = \int_{S_{r,\theta}} \alpha(x,y)ds. \tag{2}$$

Initially, let us restrict $\alpha(x,y)$ to be an isotropic parameter of interest (e.g. slope of the ultrasonic attenuation coefficient as a function of frequency) evaluated along $S_{r,\theta}$ the linear path from transmitter to receiver for view angle θ at translation position r. We further restrict $\alpha(x,y)$ to be zero outside a circular region R, bounded by $|r| \leq a$. The zero-order moment of the projection is defined as

$$M_o(\theta) = \int_{-a}^{a} p(r,\theta)dr. \tag{3}$$

Inserting the projection, Eq. (2), into the moment integral, Eq. (3), we observe that the zero-order moment is the integral of the parameter over the entire area,

$$M_o(\theta) = \int_{-a}^{a} \int_{S_{r,\theta}} \alpha(x,y)dsdr = \iint_R \alpha(x,y)dA \tag{4}$$

where dA is the differential area and R is the scan region $-a \leq r \leq a$ and $0 \leq \theta \leq \pi$. Provided that $\alpha(x,y)$ is isotropic, at any view angle, θ, the integration of $\alpha(x,y)$ yields the same result. Thus M_o is constant for all view angles θ and is a measure of the total attenuation over the entire object. This result for the parallel-ray geometry, well-known in the literature of computed tomography, applies only for the case of isotropic attenuation.

We now consider the case in which the parameter $\alpha(x,y)$ is a function of the direction of wave propagation, i.e., $\alpha(x,y)$ is anisotropic. Under these conditions $M_o(\theta)$ is no longer constant with respect to θ. To illustrate this, we consider an object exhibiting a single, linearly-directed anisotropy. Under this restriction, $C(x,y,\psi) = C(\psi_\theta)$ where the angle $\psi_\theta = (\theta-\psi)$ between the anisotropy axis and the direction of wave propagation, θ, is constant within the projection for any angle. Therefore, $M_o(\theta)$ is

$$M_o(\theta) = \int_{-a}^{a} p(r,\theta)dr = \int_{-a}^{a} \left\{ \int_{S_{r,\theta}} \alpha(x,y,\psi_\theta)ds \right\} dr \tag{5}$$

and using Eq. (1)

$$M_o(\theta) = \int_{-a}^{a} \left\{ \int_{S_{r,\theta}} \alpha_o(x,y)[1 + C(\psi_\theta)]ds \right\} dr. \tag{6}$$

In this case, since $C(\psi_\theta)$ is independent of (x,y),

$$M_o(\theta) = [1 + C(\psi_\theta)] \int_{-a}^{a} \int_{S_{r,\theta}} \alpha_o(x,y) ds\, dr \tag{7}$$

or

$$M_o(\theta) = [1 + C(\psi_\theta)]\, M_o^i \tag{8}$$

where M_o^i is the isotropic component of $M_o(\theta)$. Therefore, an object exhibiting a single linearly-directed anisotropic axis exhibits a zero-order projection-moment which is directly related to the same anisotropic angular dependence function $C(\psi_\theta)$ as the intrinsic parameter $\alpha(x,y,\psi_\theta)$. (A generalization of these results to three dimensions is considered in the Appendix.)

Intrinsic Versus Extrinsic Anisotropy

A measurement can display apparent anisotropy from sources other than the intrinsic anisotropy of the parameter measured. We refer to these effects as extrinsic anisotropy. Extrinsic anisotropy can arise from a number of sources, some of which are considered here.

a) The geometry of an actual acoustic beam differs from that of the uniform collimated pencil beam implicit in the models presented here. Except for cases of unusually high symmetry such as a circularly symmetric object located at the center of rotation of the measurement apparatus, most measurements should exhibit some extrinsic anisotropy related to beam-geometry and the location of the object.

b) The effects of refraction and diffraction can give rise to path aberrations, refractive beam displacement at the receiver, and other perturbations which cause measurements on an isotropic object to exhibit an anisotropic angular dependence.

c) The reflection loss at an acoustic impedance discontinuity is a strong function of angle, and can appear as a substantial component in apparent attenuation measurements [6-11]. We note however, that measurements based on the slope of the attenuation coefficient as a function of frequency reduce reflection losses. Therefore projections based on the slope should exhibit reduced extrinsic anisotropy compared with projections based on attenuation measured at a single frequency.

We first illustrate extrinsic anisotropy in the slope of the attenuation arising from refraction. A ray-tracing based simulation of an object exhibiting no intrinsic anisotropy was employed and reconstructions were based on the slope of the attenuation to reduce reflection losses. The results of this simulation are presented in figure 2. Panel a shows beams traced through an object exhibiting the same index of refraction as the surrounding medium. Panel b shows the corresponding results for an object exhibiting a speed of sound 5 percent higher than that of the surrounding medium. Panels c and d are the respective computed tomograms. The curve

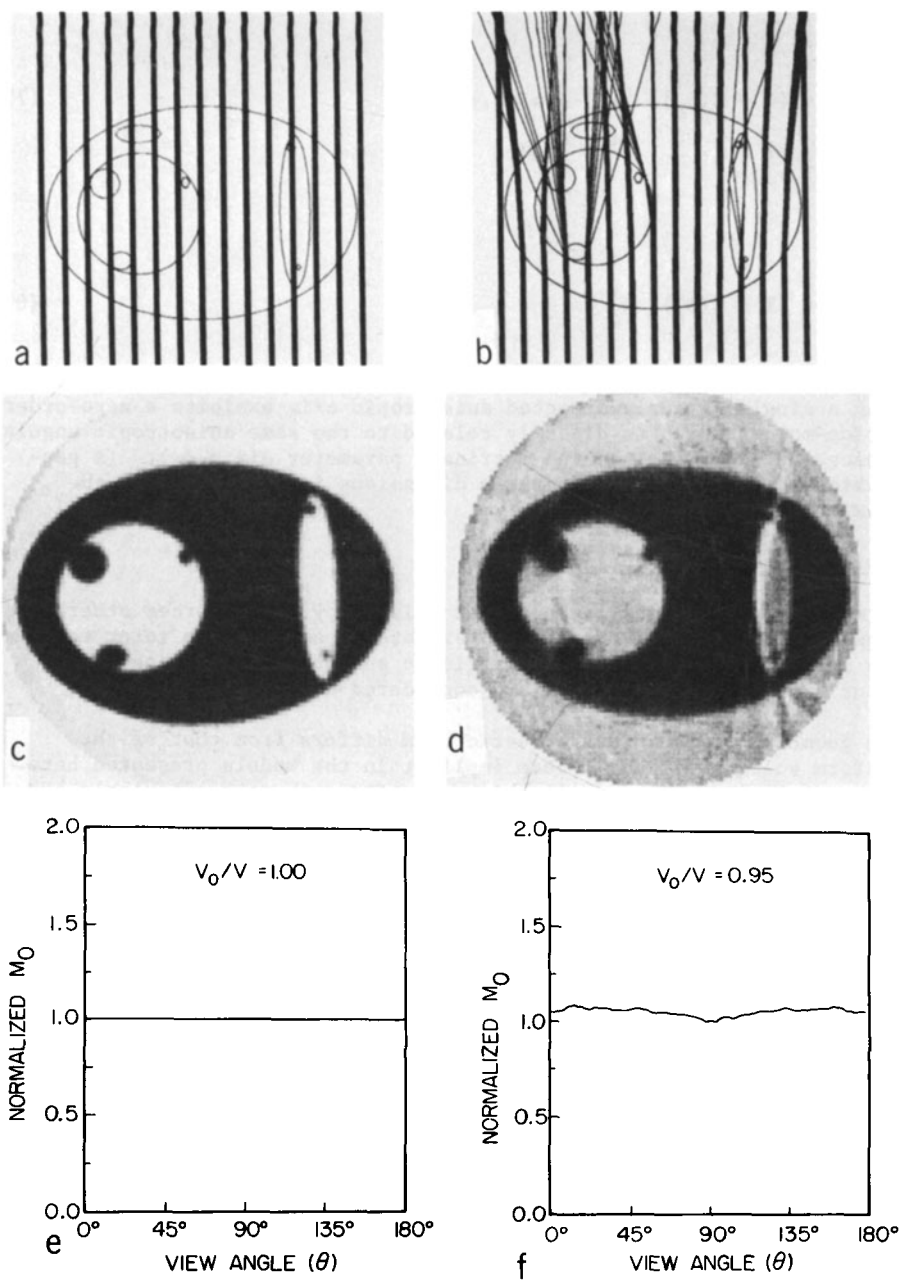

Fig. 2. Extrinsic anisotropy due to refraction is demonstrated by simulation of an intrinsically-isotropic but refracting object. Shown are: a) selected simulated beams transmitted through an object with unity refractive index; b) selected simulated beams exhibiting refraction due to 5 percent difference in the refractive index; c) tomographic reconstruction of the non-refracting simulated object; d) tomographic reconstruction of the 5 percent refracting simulated object; e) plot of the zero-order moment versus view angle for the non-refracting object; and f) plot of the zero-order moment versus view angle for the refracting object.

$M_o(\theta)$ is plotted in panel e for the non-refracting case, and in panel f for the refracting case. For purposes of illustration, all plots of $M_o(\theta)$ are normalized to the minimum value of $M_o(\theta)$ in each case. The magnitude of the extrinsic anisotropy exhibited in this example of a refracting, isotropic medium is less than 1.1 to 1.

To illustrate the experimentally observed magnitude of extrinsic anisotropy arising from all sources encountered in a typical laboratory study, we obtained projections of the attenuation at each of eight equally spaced frequencies between 3 and 7 MHz for two approximately cylindrical test objects: i) a 2 cm diameter fingercot filled with olive oil exhibiting a velocity approximately 3 percent lower than that of the surrounding water, and ii) a 5.5 cm diameter cylinder of laboratory gelatin exhibiting a velocity approximately 2 percent higher than that of water. Each of the objects was located away from the rotational center of the scanning apparatus to eliminate circular symmetry with respect to the transmitted beam. A phase insensitive acoustoelectric receiver was used to eliminate phase cancellation effects [6,7,12,13]. In figure 3, M_o based on the slope of the attenuation is plotted as a function of angle θ for both intrinsically isotropic test objects (solid and dotted curves). The extrinsic anisotropy for the slope is less than 1.1 to 1 for both objects.

To illustrate the extrinsic anisotropy due to reflection losses at acoustic impedance discontinuities, $M_o(\theta)$ based on single frequency projections of the fingercot filled with olive oil is also presented in figure 3 (dashed curve). These 3.5 MHz projections comprised part of the 8-frequency projection data set used to produce the $M_o(\theta)$ plot for the slope (dotted curve). The 1.4 to 1 anisotropy of the single frequency projections is considerably larger than the 1.1 to 1 anisotropy exhibited by the slope, presumably due to reflection loss at impedance discontinuities. This underscores the utility of the frequency dependence of attenuation as a means for separating the components of reflection loss from attenuation measurements [6]. Consequently, projections based on the slope were employed in the remainder of this study to infer the intrinsic anisotropy of attenuation in media such as tissue which exhibit an approximately linear frequency dependence of attenuation. A comparison of the results of simulations of refracting but intrinsically isotropic objects (Fig. 2) and experimental measurements of phantoms made of refracting, isotropic media such as olive oil and gelatin (Fig. 3) suggest that the extrinsic anisotropy encountered in measurements on soft tissue may be of the order of 1.1 to 1. The modest magnitude of extrinsic anisotropy is in marked contrast to the substantial magnitude of intrinsic anisotropy observed in the slope of attenuation in some tissues as discussed below.

In a previous publication we reported results illustrating the anisotropy exhibited by a segment of excised dog heart [6]. The section was approximately rectangular in cross-section, 0.9 by 1.8 cm, and was cut from the left ventricular wall in the region between the two papillary muscles. This corresponds to the same location as in an extensive series of measurements reported by O'Donnell et al. [14] on excised dog hearts. The slope of the attenuation was computed from eight measurements ranging from 3 to 6.5 MHz in 500 kHz steps, and was compensated for the frequency dependence of the transmitted beam width [6]. The 0° and 180° projection angles corresponded to propagation along the apparent muscle fiber direction; the 90° and 270° views were perpendicular to the apparent muscle fiber direction. An average of data from 30 sites measured perpendicular to the muscle fiber yielded 0.073 ± 0.017 $cm^{-1}MHz^{-1}$ (mean $\pm$ S.E.), in good agreement with the results of previous measurements, 0.072 ± 0.001 $cm^{-1}MHz^{-1}$ [14]. The value measured parallel to the muscle fiber was 0.19 ± 0.02

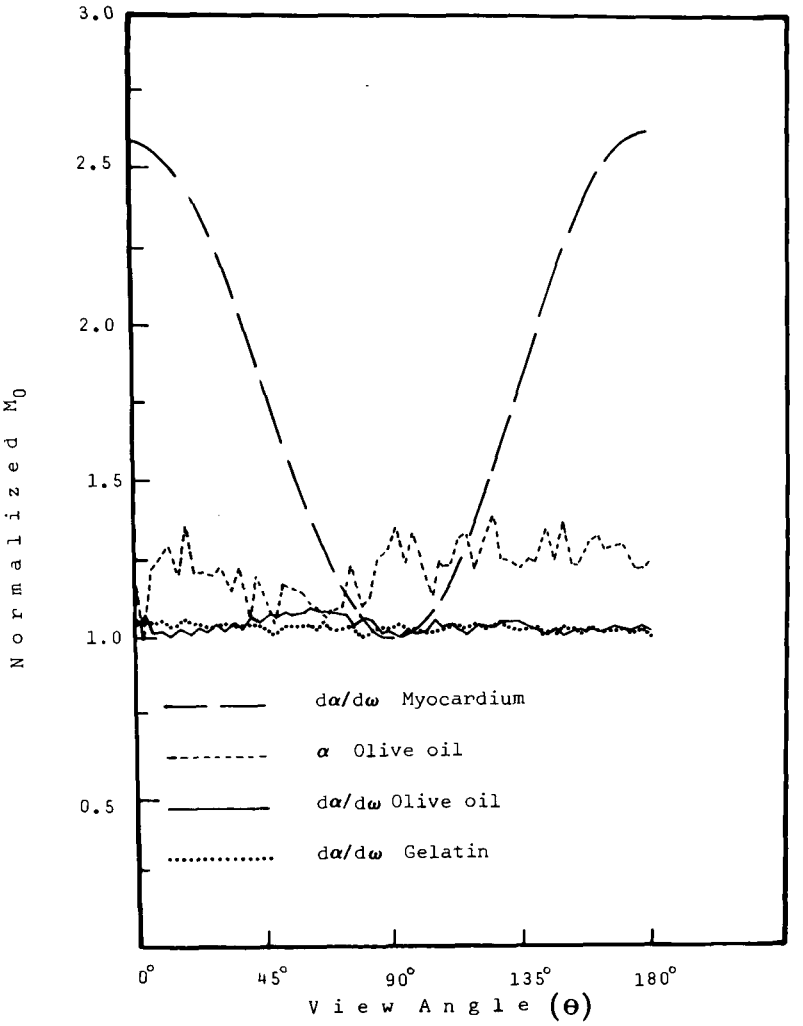

Fig. 3. Extrinsic anisotropy for intrinsically isotropic phantom objects is compared to the intrinsic anisotropy of myocardial tissue. The zero-order moment is plotted versus angle over 180° of view based on: a) slope of the attenuation in a fingercot filled with olive oil, 3 percent refraction (solid line); b) slope of the attenuation in a cylinder of laboratory gelatin with a small off-center hole, 2 percent refraction (dotted line); c) attenuation measured at 3.5 MHz in the fingercot filled with olive oil (short dashes); and d) slope of the attenuation in excised dog myocardium reported in reference [6] (long dashes). The axes are scaled so that the smallest measurement in each graph corresponds to the value 1; the maximum values attained represent the anisotropy ratios.

and exceeded that measured perpendicular to the fibers by the factor of 2.6 to 1. The zero-order moment $M_0(\theta)$ of the slope of attenuation in the sample exhibited 180° periodicity, and was well approximated by an empirical function of the form $A + B \cos(2\psi_\theta)$ [6]. This curve is illustrated in figure 3 for comparison with the $M_0(\theta)$ plots for the intrinsically isotropic

objects. The parameters A and B of the empirical anisotropy characterization were selected to yield the same minimum and maximum values of $M_o(\theta)$, and result in the same anisotropy ratio $(A + B)/(A - B) = 2.6$. Because the muscle fibers in heart do not all lie in the plane in which the measurements were made [15,16], the 2.6 to 1 anisotropy may reflect a lower bound on the value which would be observed if all fibers were confined to the plane of measurement (see Appendix). The functional form of the anisotropy remains the same, however, provided that the projections of the fibers onto the plane are aligned in a single direction.

Motivated by the measurements on myocardium we chose $C(\psi)$ in Eq. (1), the empirical model for intrinsic anisotropy, to be sinusoidal, periodic in 180°, and of magnitude β,

$$C(\psi_\theta) = \beta(1 + \cos(2\psi_\theta))/2 = \beta \cos^2(\psi_\theta). \tag{9}$$

For linearly-directed anisotropy and a wave traveling in the θ direction,

$$\alpha_a(x,y,\psi_\theta) = \alpha_o(x,y)\,[1 + \beta \cos^2(\psi_\theta)] \tag{10}$$

where $\alpha(x,y)$ is the isotropic component of the parameter, and β is the magnitude of the anisotropy. Using this model, the anisotropy ratio is then $(1 + \beta)$ to 1.

II. Tomographic Reconstruction of Projections Exhibiting Anisotropy

Images of tissue have been reconstructed from ultrasonic attenuation measurements using filtered back projection algorithms [6-8, 17-19] and iterative algebraic algorithms [20-22]. We chose to investigate effects of anisotropy on tomographic reconstruction using filtered back projection because the filtered back projection algorithm can be expressed analytically, permitting the expression of anisotropic effects in closed analytical form for simple geometries. In this section, the projections for an annulus are derived analytically for both linearly-directed and tangentially-directed anisotropy geometries. The resulting filtered back projection reconstructions are then derived analytically for the linearly-directed case. The effects of anisotropy for more complicated geometries are demonstrated by computer reconstruction of computed projections. Predictions of the effects of anisotropy on computed tomography based upon models and simulations presented here are compared with results for reconstructions made from measurements on tissue.

Projections and Reconstruction of a Disc and an Annulus Exhibiting Linearly Directed Anisotropy

Within an isotropic, uniform medium, the linearized projection measurement is proportional to the path length within the object. The proportionality constant is the parameter, α_o, to be reconstructed. (Assumptions of a uniform collimated beam and the absence of refraction or reflection are implicit.) For a disc of radius a (see Fig. 4) the measurement at position r for any angle is:

$$p_i(r) = 2\,a\,\alpha_o \sqrt{1 - (r/a)^2}\; u(a - |r|) \tag{11}$$

where

$$u(\tau) = \begin{cases} 0 & \tau < 0 \\ 1 & \tau \geq 0 \end{cases}. \tag{12}$$

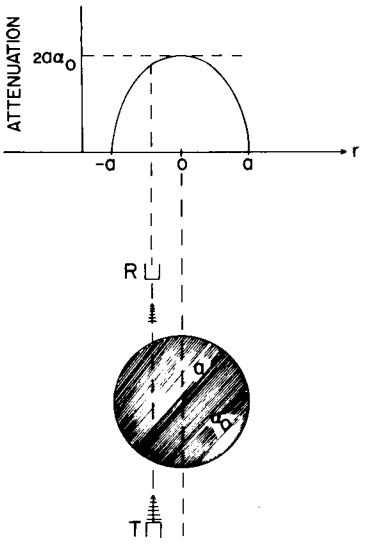

Fig. 4 Measurement of the tomographic projection of a disc-shaped object is shown in this schematic representation. The geometry of the transmit-receiver axes and the projection corresponding to an isotropic, homogeneous disc are illustrated.

Using the linearly-directed anisotropy model, Eq. (10), the anisotropic disc projection measurement is

$$p_a(r,\theta) = p_i(r) \quad [1 + \beta \cos^2(\psi_\theta)]. \tag{13}$$

We summarize the sequence of steps followed in analytically applying conventional filtered-back projection reconstruction:

1) Fourier transform $p(r,\theta)$ in r,

$$P(f,\theta) = \int_{-\infty}^{\infty} p(r,\theta) e^{-i2\pi fr}\, dr. \tag{14}$$

2) Spatially filter $p(r,\theta)$ by multiplying in the spatial frequency (f) domain,

$$G(f,\theta) \equiv P(f,\theta) \quad |f| \tag{15}$$

where $|f|$ is the well known filtered back-projection inverse filter [23,24].

3) Inverse Fourier transform $G(f,\theta)$ in f,

$$g(r,\theta) = \int_{-\infty}^{\infty} G(f,\theta)\, e^{i2\pi fr}\, df. \tag{16}$$

4) Back project $g(r,\theta)$ to reconstruct $\hat{\alpha}(r,\theta)$,

$$\hat{\alpha}(r,\theta) = \int_0^{\pi} g\,(r\cos(\theta-\theta'),\theta')\,d\theta'. \tag{17}$$

Applying the above algorithm to the isotropic projections of Eq. (11) we obtain the expected isotropic disc,

$$\hat{\alpha}_i(r,\theta) = \alpha_o u(a-|r|). \tag{18}$$

In contrast, application of the above to projections of the linearly-directed anisotropic disc, Eq. (13), results in the double integral

$$\hat{\alpha}_a(r,\theta) = \alpha_o\,[1 + 2\,a\,\beta \int_0^{\pi}\int_{-\infty}^{\infty} P(f,\theta')|f|\; e^{i2\pi fr\cos(\theta-\theta')}\,dfd\theta'] \tag{19}$$

where $P(f,\theta')$ is the one-dimensional Fourier transform of the anisotropic component of the projection,

$$P(f,\theta') = \alpha_o\,\beta a\cos^2(\theta')J_1(2\pi fa)/f. \tag{20}$$

Exchanging the order of integration to perform the θ integration first, and using a series expansion of $\cos[2\pi f\, r\cos(\theta-\theta')]$ in terms of Bessel functions [25] we obtain the analytical result

$$\hat{\alpha}_a(r,\theta) = \hat{\alpha}_i(r,\theta) + \alpha_o\beta \begin{cases} 1/2 & r < a \\ (1/2)-\cos(2\theta)/4 & r = a \\ (a^2/r^2)\cos(2\theta) & r > a \end{cases} \tag{21}$$

A reconstruction of a disc exhibiting linearly-directed anisotropy is presented in figure 5a. The image was obtained by computer reconstruction of the anisotropic projections of Eq. (13). The disc is characterized by 2 to 1 anisotropy, with isotropic component $\alpha_o = 1$ and anisotropy magnitude $\beta = 1$. The reconstruction from the projections is in agreement with the analytical result of Eq. (21). The reconstruction exhibits the predicted 2θ angular variation of the $1/r^2$ decaying error outside the disc. Likewise, inside the disc, a constant $\alpha_o(1 + \beta/2)$ is reconstructed.

Results for the case of an annulus exhibiting linearly-directed anisotropy can be obtained from Eq. (21) by the linear superposition of two concentric discs of radii a_1 and a_2, respectively.

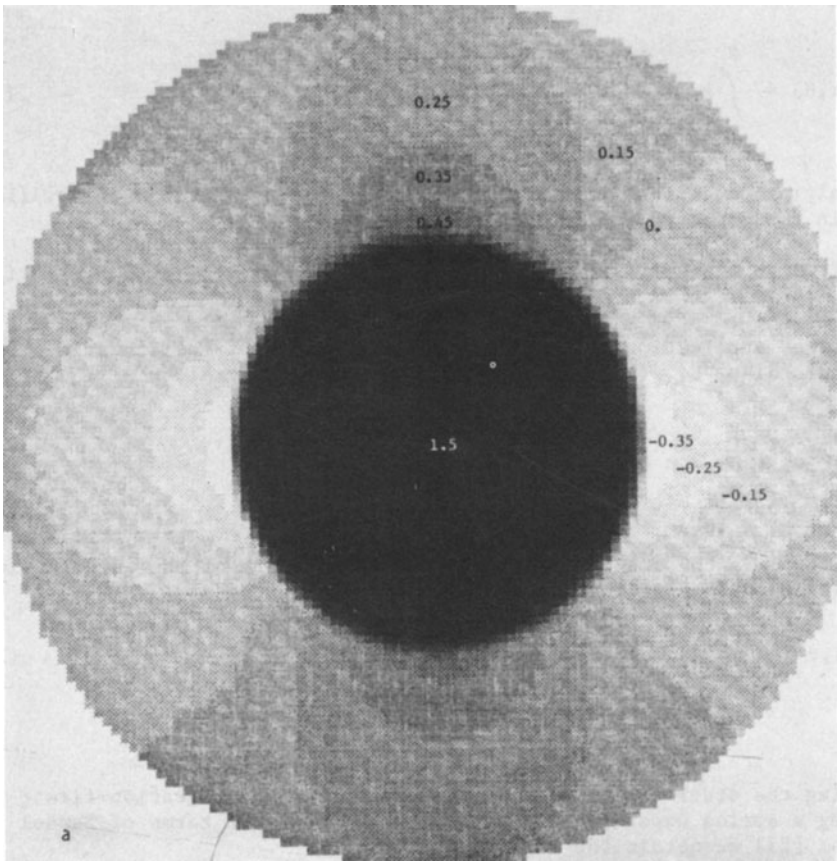

Fig. 5. The images shown were reconstructed from simulated projections of a linearly-directed anisotropic disc in panel a, and annulus in panel b. Both simulated objects possess an isotropic component $\alpha_o = 1.0$, and 2 to 1 anisotropy ($\beta = 1$). The reconstructed images are in agreement with the analytical results of Eqs. (21) and (22) respectively.

$$\hat{\alpha}_a(r,\theta) = \hat{\alpha}_i(r,\theta) + \alpha_o\beta \begin{cases} 0 & r < a_2 < a_1 \\ \cos(2\theta)/r & r = a_2 \\ (1/2)-(a_2^2/r^2)\cos(2\theta) & a_2 < r < a_1 \\ (1/2)-[(1/4)+(a_2^2/r^2)]\cos(2\theta) & r = a_1 \\ [(a_1^2/r^2)-(a_2^2/r^2)]\cos(2\theta) & a_2 < a_1 < r \end{cases} \quad (22)$$

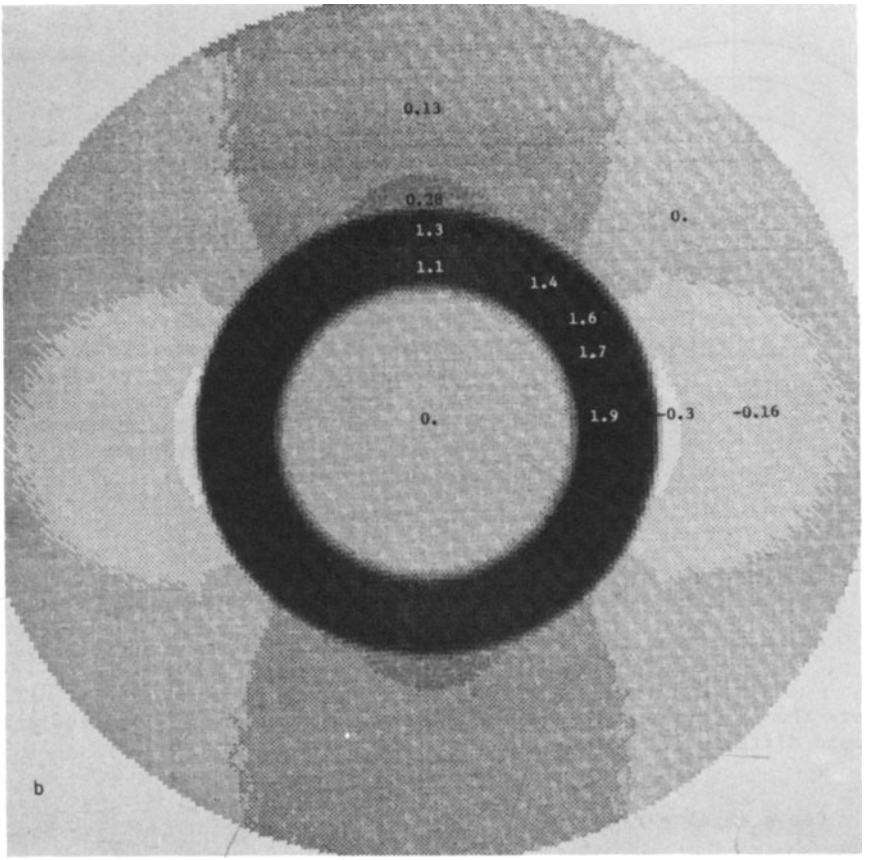

Figure 5 - Continued

Figure 5b illustrates the result of computer reconstruction of analytically derived projections obtained from Eq. (13) for the linearly-directed anisotropic annulus. The values $\alpha = 1$ and $\beta = 1$ for the annulus are the same as those for the disc in figure 5a. The computer reconstruction obtained from the projections exhibits all of the features predicted by the analytical result is given in Eq. (22). In particular, as indicated in Eq. (22), the center of the annulus reconstructs without error to 0.

Tangentially-Directed Anisotropy in the Annulus

We now consider a second geometrical class of anisotropy which occurs when the local anisotropy axes are parallel to continuous curves in space. This tangential anisotropy geometry is illustrated schematically in figure 6. Because of the circular symmetry of the disc and its concentric anisotropy axes, tomographic projections of the disc are independent of view angle θ in spite of the intrinsic anisotropy of the object. Every straight-line path through the disc forms an angle $\psi_\theta(r,s)$ with respect to an anisotropy axis which continuously varies with position along the path. If we denote by s the position along the path from transmitter to receiver, then at transmit-receive position r within the disc the differential measurement at s is

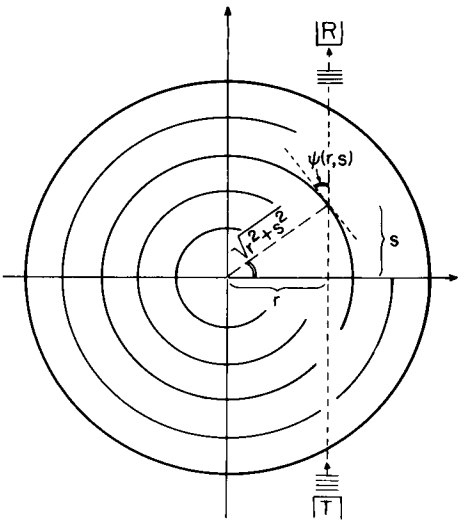

Fig. 6. This schematic diagram illustrates key features in the derivation of the projection of a disc exhibiting tangentially-directed anisotropy. The transmitter and receiver are located at position r. The tangent to the curved anisotropy axis at (r,s) representing the direction of anisotropy is shown. The angle $\psi_\theta(r,s)$ between the anisotropy axis and the direction of propagation at (r,s) is given by $\cos(\psi_\theta(r,s)) = r/(r^2+s^2)^{1/2}$.

$$dp_a = \alpha_o(1 + \beta \cos^2 [\psi_\theta(r,s)])ds \tag{23}$$

where the anisotropy along ds is modeled as the linearly-directed anisotropic differential volume shown in figure 1a. From geometry

$$\cos \psi_\theta(r,s) = r/(s^2 + r^2)^{1/2} \tag{24}$$

and hence, the projection is

$$p_a(r,\theta) = 2 \int_0^{\sqrt{a^2-r^2}} \alpha_o [1 + \beta r^2/(s^2 + r^2)] \, ds \quad 0 \leq \theta \leq 2\pi. \tag{25}$$

Thus,

$$p_a(r,\theta) = p_i(r) + 2\alpha_o\beta|r|\tan^{-1}\left\{\sqrt{(a/r)^2-1}\right\} u(a-|r|) \tag{26}$$

where $p_i(r)$ is the projection from the isotropic disc. Corresponding projections for an annulus are derived from Eq. (26) using superposition.

In figure 7a, we illustrate reconstruction of a tangentially anisotropic disc exhibiting the projection given by Eq. (26). The isotropic and anisotropic components are $\alpha_o = 1$ and $\beta = 1$ respectively. Numerical values shown in figure 7a represent local averages.

We now examine an annulus exhibiting tangential anisotropy. As an example of an annular object that might exhibit tangential anisotropy we

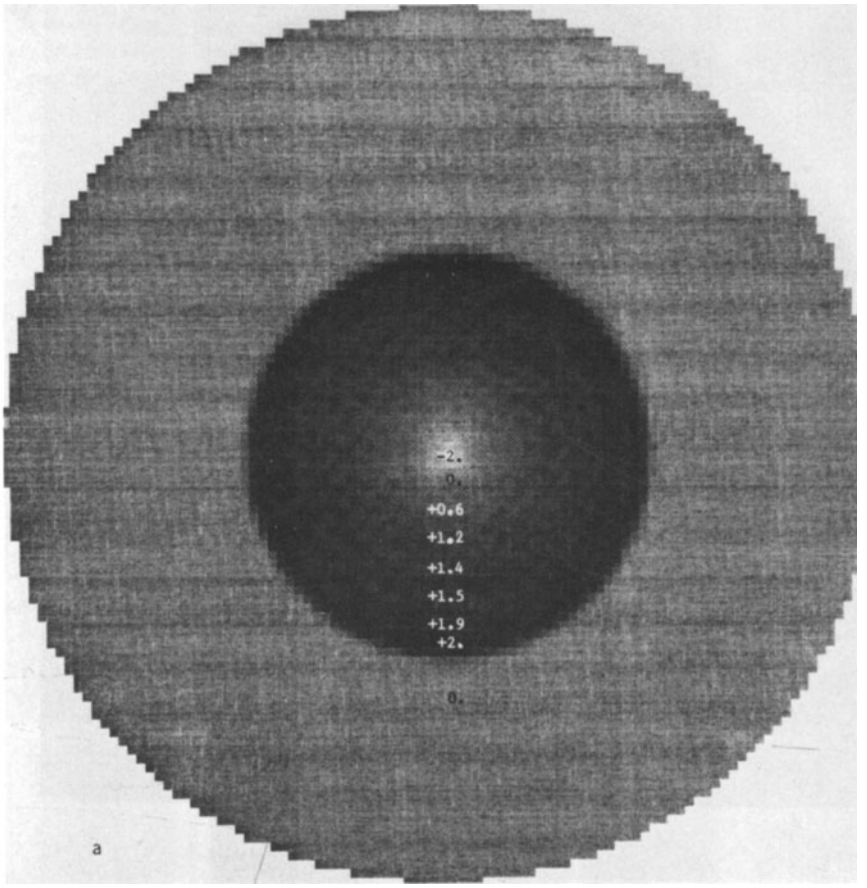

Fig. 7. The images shown were reconstructed from simulated projections of a tangentially-directed anisotropic disc in panel a, and annulus in panel b. Both simulated objects possess an isotropic component α_o = 1.0 and 2 to 1 anisotropy (β = 1) oriented as concentric rings about the center. The regions outside the objects reconstruct to the correct value of zero. The empty region inside the annulus reconstructs to a consistent -0.4 instead of zero. The annulus reconstructs to values larger than the isotropic component, α_o.

consider a crude model of the left ventricle of a heart consisting of layers of muscle tissue wrapped concentrically around a fluid filled chamber. [14,15] For α_o = 1 and β = 1, the analytically derived projections are reconstructed in figure 7b. As in the case of the disc, the correct value of zero is reconstructed outside the object. This result for tangentially directed anisotropy is in contrast with that obtained for the linearly-directed anisotropic disc and annulus (Fig. 6), outside of which considerable error occurs. The annulus reconstructs to its largest value (1.9) near the outer edge and the values decrease toward the inner edge with a decay similar to that within the disc in figure 7a. A uniform negative value

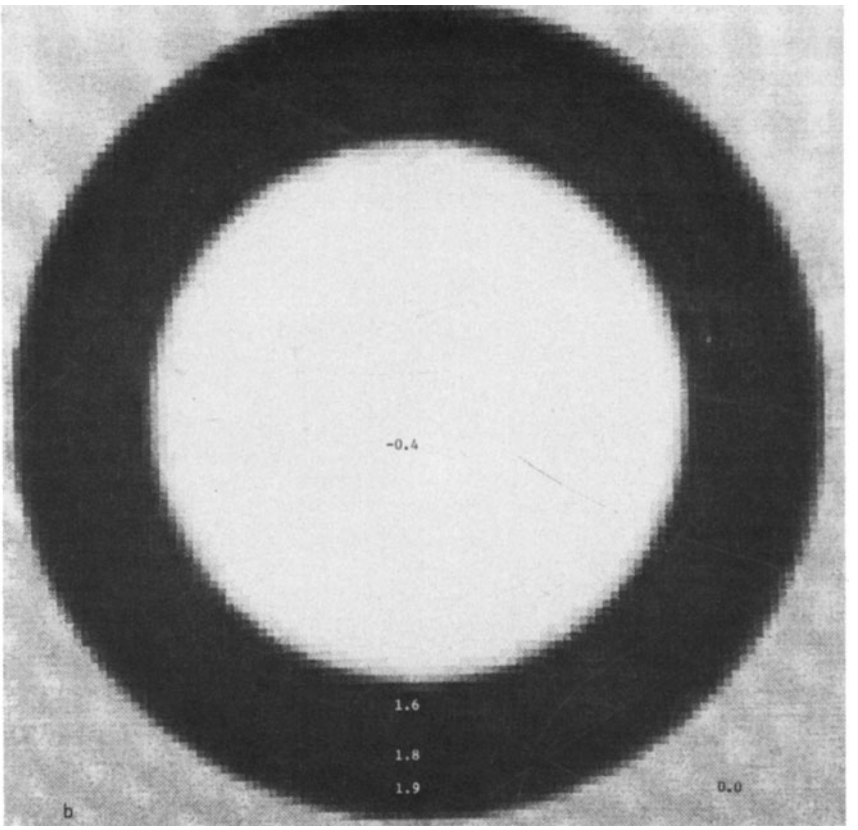

Figure 7 - Continued

(-0.4) is reconstructed inside the annulus. The predicted negative value is quite significant, as discussed in a subsequent section.

Simulations of Elliptically Shaped Regions

In order to estimate the effects of anisotropy on the tomographic reconstructions of objects such as tissue specimens, more complicated object geometries were simulated. Elliptically shaped regions, each possessing particular values of isotropic attenuation, α_o, anisotropy magnitude β, and linearly-directed anisotropy axis orientation, were superimposed to simulate complicated structures.

To illustrate the potential effects of an anisotropic region on neighboring isotropic regions, a single anisotropic ellipse of 2 to 1 anisotropy magnitude (β = 1) is reconstructed in figure 8. The substantial positive and negative errors surrounding the ellipse are expressed as a percentage of the value reconstructed within the ellipse. Objects adjacent to the long sides of the ellipse will reconstruct with underestimated attenuation values owing to the negative values on either side of the ellipse. Near the ends of the ellipse, objects will reconstruct with overestimated atten-

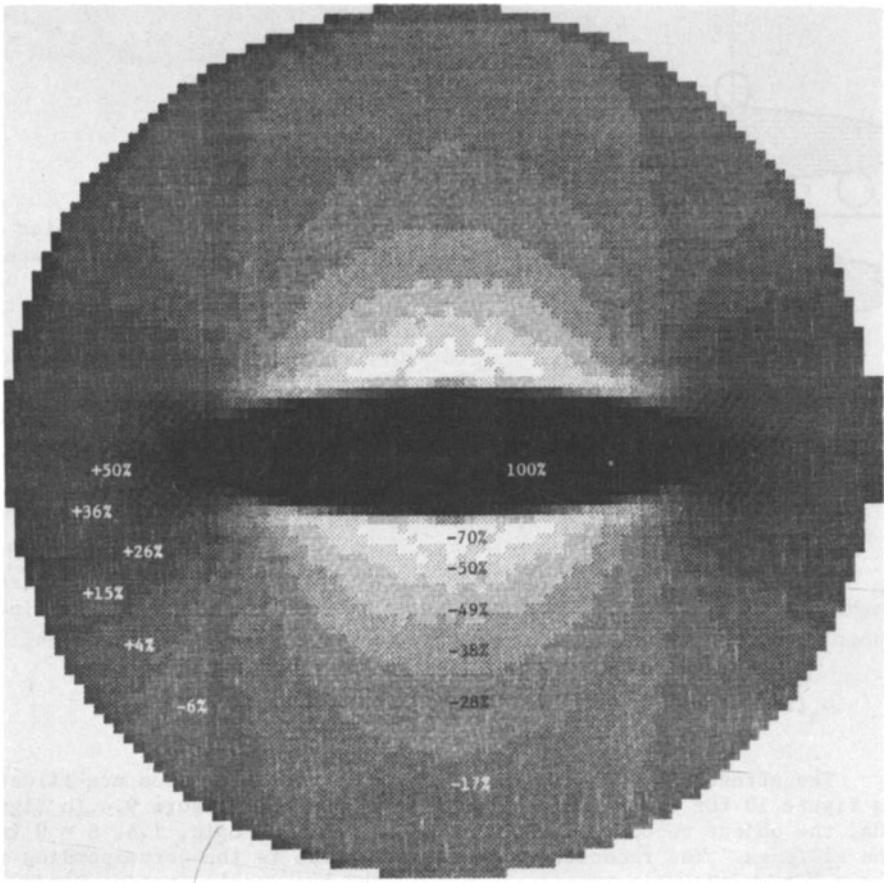

Fig. 8. The effect of 2 to 1 linearly-directed anisotropy in an isolated ellipse is demonstrated in this tomographic reconstruction. Reconstructed values outside the ellipse are expressed as a percentage of the value reconstructed in the ellipse; these values differ from the correct value of zero due to the anisotropy of the ellipse.

uation values. Qualitatively, errors of both signs occur because the reconstruction algorithm evenly weights each projection. Hence, the views with a larger attenuation (parallel to the anisotropy axis) back project with a larger magnitude than the views at other angles and incomplete cancellation outside the object yields positive errors. Similarly, lower attenuation views back project with a value which is more than cancelled by the other views yielding negative errors.

In figure 9 we present a schematic diagram of one superimposed circle-and-ellipse geometry that was reconstructed to illustrate a more complicated geometry. All circles possess an isotropic attenuation $\alpha_o = 0.5$. The two ellipses are characterized by a linearly-directed anisotropy parallel to the lines shown. Each ellipse has an isotropic component of attenuation

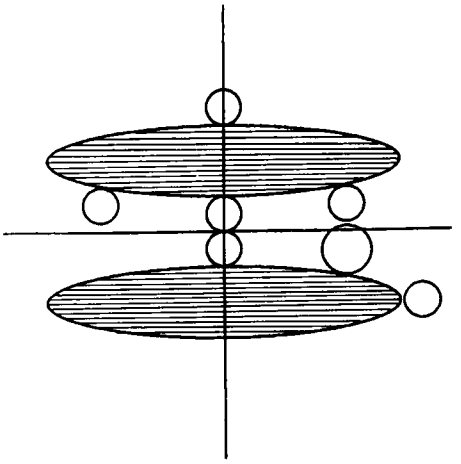

Fig. 9. The collection of circular and elliptic objects shown schematically here are used subsequently to demonstrate the effects of anisotropic objects in a tomographic reconstruction. The circular objects are intrinsically isotropic ($\beta = 0$), with $\alpha_o = 0.5$. The ellipses exhibit 2 to 1 anisotropy ($\beta = 1$) with linearly-directed axes parallel to the lines shown, and an isotropic component $\alpha_o = 0.5$.

$\alpha_o = 0.5$, equal to that of the surrounding discs. The 2 to 1 anisotropy magnitude ($\beta = 1$) causes the attenuation measured parallel to the lines shown to appear twice as large as that measured normal to the lines,

$$\alpha_a(x,y) = 0.5\ (1 + \cos^2 \psi_\theta). \tag{27}$$

The effects of anisotropic regions on adjacent regions are illustrated in figure 10 for the collection of regions shown in figure 9. In figure 10a, the object reconstructed had all regions isotropic, i.e. $\beta = 0$ in the ellipses. The reconstruction in figure 10b is the corresponding result for $\beta = 1$ in the anisotropic ellipses. The grey scale imaging window for panels a and b was selected with the $\alpha_o = 0.5$ value at mid range so as to show both over- and under-estimations of the reconstructed attenuation. Numerical values represent local averages of the reconstructed attenuations.

From the simulations presented in figures 8 and 10 and from other simulations, the following conclusions may be drawn:

1) The attenuation (or slope of the attenuation) values reconstructed within isolated anisotropic regions lie in the range between α_o and $\alpha_o(1+\beta)$, and are functions of the object geometry. The isolated ellipse of figure 8 had a major-to-minor axis ratio of 5 to 1 and reconstructed to approximately $\alpha_o(1+\beta)$. In another simulation, not shown, a 5 to 3 ellipse geometry reconstructed to $\alpha_o(1 + 0.6\beta)$. Finally, the disc in figure 5 reconstructed to $\alpha_o(1 + 0.5\beta)$. These three examples of identical 2 to 1 anisotropy demonstrate the geometry dependence of the values reconstructed in the anisotropic region.

2) Objects adjacent to anisotropic regions can suffer either over- or under-estimation, depending upon the anisotropy magnitude and geometry. The negative estimation errors affected not only the isotropic discs shown in figure 10, but also the neighboring anisotropic ellipse. The interaction of the anisotropic ellipses resulted in reconstructed values of 0.9 whereas the isolated ellipse in figure 8 reconstructed to 1.0.

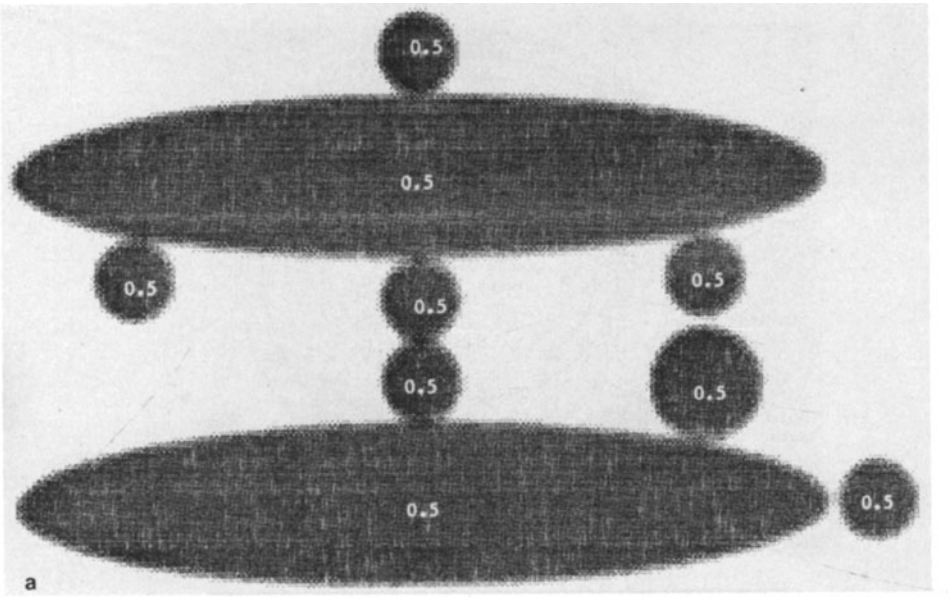

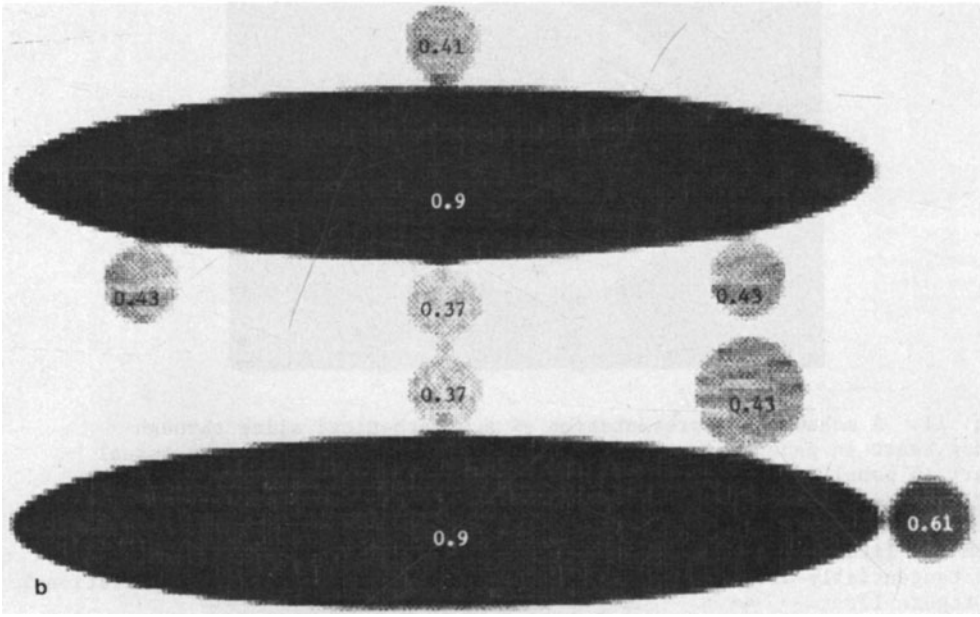

Fig. 10. The collection of simulated objects in figure 9 are reconstructed here. Panel a shows the objects reconstructed from simulated projections in which all objects were taken to be intrinsically isotropic (i.e., $\beta = 0$). In panel b the ellipses were taken to be anisotropic with $\beta = 1$. The anisotropy of the ellipses caused the isotropic discs to suffer both over- and under-estimation.

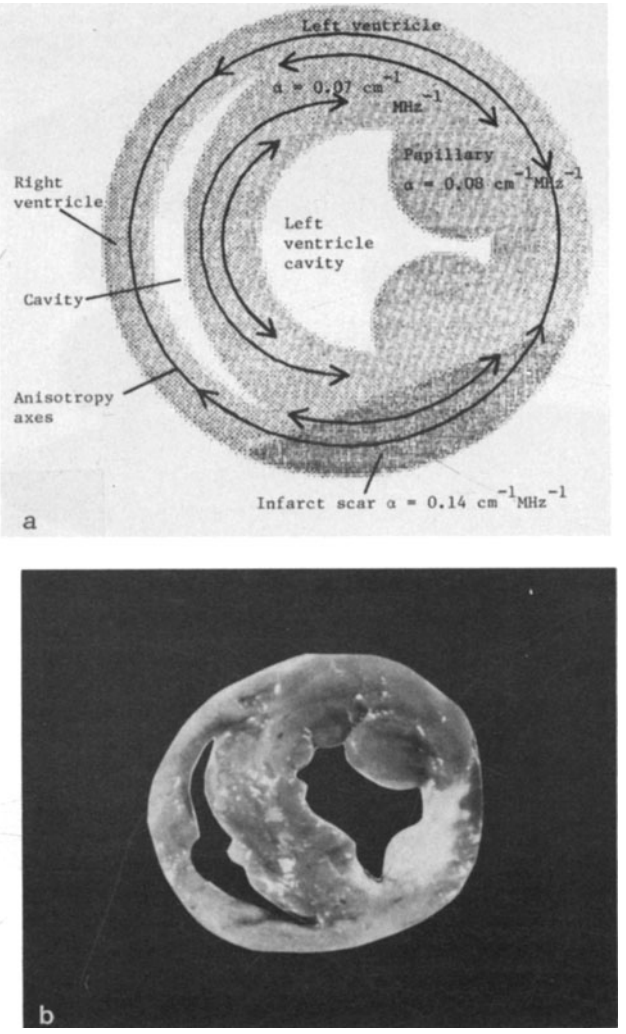

Fig. 11. A schematic representation of a hypothetical slice through a dog heart in panel a is to be compared with a photograph of an actual heart in panel b. The white fibrous region of the heart in panel b corresponds to scar tissue from an experimentally induced infarct. The values shown in panel a represent values of the slope of attenuation from the literature [14,26,27]. Anisotropy axes in panel a represent the tangentially-directed anisotropy geometry values used in the simulations in figure 12.

3) Although the errors in the reconstructed values resulting from anisotropy can be substantial, the objects reconstruct to qualitatively correct geometries in the presence of modest anisotropy. Geometrical distortions result from both negative errors which can obliterate some regions and positive errors which can distort and extend edges.

Tomography of the Heart

A recent tomographic study from our laboratory of dog hearts *in vitro* [6] demonstrated the capability of delineating regions of infarct in images based on attenuation and on time-of-flight measurements. We now address the implications of anisotropy for attenuation images of the heart of this sort. We carried out simulations based upon the 2.6 to 1 anisotropy observed in myocardium and the model presented here. The simulated object used in our investigations, presented schematically in figure 11a, is a representation of a hypothetical slice through the ventricles of a dog heart. A photograph of an actual heart is presented in figure 11b. The photograph reveals the right and left ventricular cavities, papillary muscles in the left ventricle, and a white fibrous region in the posterior left ventricle corresponding to scar from a myocardial infarct experimentally induced approximately 7 months prior to the study of the heart *in vitro*. The plane of the image is oriented approximately perpendicular to the septum. Within the layers of the left ventricular myocardium, muscle fibers are known to be oriented in various directions parallel to or slanted slightly out of the plane of the image [15,16]. As a simplification, we model the fibers as parallel to the plane of the image. The papillary muscle fibers are modeled as perpendicular to the plane [15]. Thus projection measurements of the slice in this plane will view anisotropic myocardium in the ventricles and septum. However, the interrogating wave propagates approximately normal to the papillary muscle fibers for all view angles, and therefore papillary muscle will appear isotropic.

In light of the geometry dependence of anisotropy effects, we investigated the potential effects of anisotropy in tomographic reconstruction of the heart with a simulated model of the heart slice shown in figure 11a. In figure 12a, we present a reconstruction of the slope of attenuation for the heart model with the intrinsic anisotropy set equal to zero (i.e., for $\beta = 0$). Slope values correspond to independent measurements [14,26,27] made in transmission at normal incidence to the muscle fibers and are summarized in figure 11a. The effect of a 2.6 to 1 tangentially-directed anisotropy is illustrated in figures 12b and 12c. Because the anisotropy of scar resulting from infarct has not been well characterized, we simulate scar with 2.6 to 1 tangentially-directed anisotropy ($\beta = 1.6$) in panel b and simulate isotropic ($\beta = 0$) scar in panel c. The isotropic components of the slope of attenuation (α_0) in all regions are equal to the normal-incidence slope values employed in the isotropic heart in panel a. The tangentially-directed anisotropy model was employed with 2.6 to 1 anisotropy oriented along the circular axes shown in figure 11a.

For comparison, a reconstructed image of actual tissue is given in figure 13a, based upon the slope of attenuation measured in the heart shown in figure 11b. An image-raster-line is plotted in figure 13b corresponding to the black line through the image in panel a. The raster-line plots the slope for regions in the surrounding medium, normal left ventricle (left), papillary muscle, the fluid contained in the left ventricle cavity (center), and scar (right).

To a first approximation, the left ventricular muscle is an elongated strip of anisotropic material much like the anisotropic ellipses of figures 8 and 10. As a result, regions reconstructed adjacent to the muscle might be expected to suffer either over or underestimation due to anisotropy. Furthermore, the entire ventricle resembles the tangentially-directed anisotropic annulus which was demonstrated in figure 7b to exhibit significant negative error inside, but no error outside. Thus one would expect no significant errors outside the heart, but papillary muscles inside might be underestimated due to negative errors there. The anisotropic

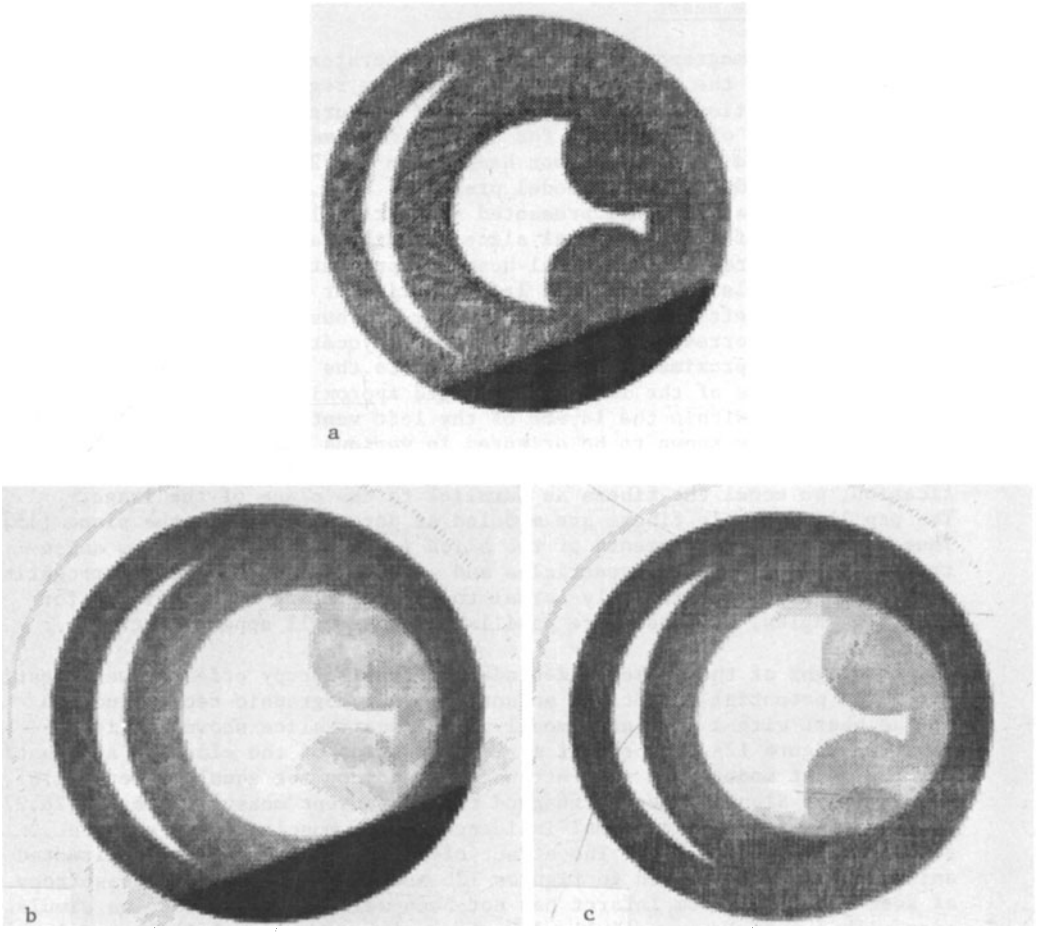

Fig. 12. Simulated projections of a hypothetical dog heart are reconstructed to form images: a) an intrinsically-isotropic model of a heart; b) a tangentially-directed anisotropic heart with infarct modeled as anisotropic; and c) a tangentially-directed anisotropic heart with infarct modeled as intrinsically-isotropic. A 2.6 to 1 anisotropy was employed with values of α_o equal to the slope values shown in figure 11a.

left ventricular muscle should reconstruct to an attenuation value lying between those along and those perpendicular to the muscle fibers.

A comparison of the reconstruction of actual heart and the simulated heart yield the following observations (a summary is given in table I). Reconstructed values are local averages given in terms of the mean $\pm$ standard deviation; values corresponding to independent measurements are quoted as the mean $\pm$ standard error of the mean.

a) The slope of attenuation in the left ventricle between the papillary muscles reconstructed to 0.15 ± 0.02 $cm^{-1}MHz^{-1}$ in the actual heart, approximately twice the value 0.072 ± 0.001 $cm^{-1}MHz^{-1}$ reported for

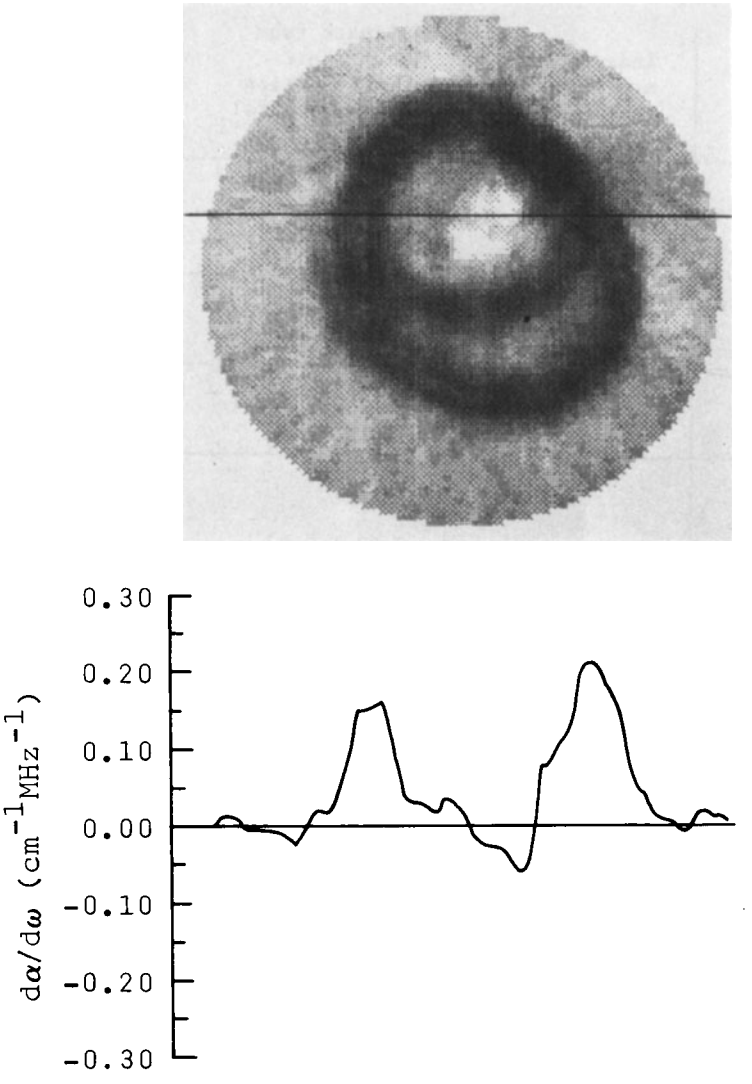

Fig. 13. Projections of the slope of attenuation in the heart studied in vitro shown in figure 13b are reconstructed to form the image shown. A plot of the image-raster line corresponding to the line through the image shows representative reconstructed values. From left-to-right one observes surrounding medium (approximately lossless), normal left ventricular muscle (overestimated), papillary muscle (underestimated), fluid (approximately lossless but reconstructs to a negative slope), and left ventricular muscle and scar tissue (overestimated).

Table I. Comparison of errors in tomography of dog heart with errors predicted by simulation of anisotropy

Anatomical site	Independent measurement[a] ($cm^{-1}MHz^{-1}$)	Estimate from tomographic reconstruction of experimental data[b] ($cm^{-1}MHz^{-1}$)	Estimate from tomographic reconstruction of simulated data[b] ($cm^{-1}MHz^{-1}$)
Normal left ventricular myocardium	0.072 ± 0.001[c] (N = 245)	0.15 ± 0.02	0.18 ± 0.01
Left ventricular infarct	0.158 ± 0.010[d] (N = 5)	0.27 ± 0.05	0.31 ± 0.01
Left ventricular papillary muscle	0.079 ± 0.002[e] (N = 21)	0.03 ± 0.01	0.03 ± 0.01
Fluid in left ventricular cavity	~0.0	-0.03 ± 0.02	-0.07 ± 0.01

[a]Measurements (mean $\pm$ standard error of the mean) of muscle were made in transmission, normal to the predominant fiber orientation. Measurements of infarct were made in transmission, normal to the epicardial surface.
[b]Local averages (mean $\pm$ standard deviation). [c]See ref. [14]. [d]See ref. [26]. [e]See ref. [27].

transmission at normal incidence to the muscle fibers [14]. In the corresponding region of the simulated heart, the value of the slope was 0.18 ± 0.01 $cm^{-1}MHz^{-1}$.

b) Isotropic regions such as the papillary muscles and fluid within the cavity of the left ventricle are surrounded by approximately tangentially-directed anisotropic media, and reconstruct to severely underestimated or negative slope values. In actual heart, the papillary muscles reconstructed to 0.03 ± 0.01 $cm^{-1}MHz^{-1}$ and simulation yielded 0.03 ± 0.01 $cm^{-1}MHz^{-1}$. Independent (non-tomographic, transmission) measurements of papillary muscle at this location indicate 0.079 ± 0.002 $cm^{-1}MHz^{-1}$ [27]. The surrounding medium and fluid within the ventricle are approximately lossless for the path lengths and frequencies used. In the heart reconstruction, the slope in the left ventricular cavity was -0.03 ± 0.02 $cm^{-1}MHz^{-1}$ in the actual heart and -0.07 ± 0.01 $cm^{-1}MHz^{-1}$ in the simulated heart.

c) Scar in the left ventricle following seven months of ischemia exhibited a slope of attenuation measured non-tomographically in the range $0.158 \pm$ $cm^{-1}MHz^{-1}$ [26] for normal incidence to the epicardial surface. Nearly twice this value, 0.27 ± 0.05 $cm^{-1}MHz^{-1}$, was reconstructed in the actual heart. Simulation of scar, based upon an isotropic model with a slope of 0.15 $cm^{-1}MHz^{-1}$, yields a reconstructed value of 0.16 ± 0.01 $cm^{-1}MHz^{-1}$. In contrast the same scar modeled with an isotropic component of slope of 0.15 $cm^{-1}MHz^{-1}$ and tangentially-directed anisotropy yields 0.31 ± 0.01 $cm^{-1}MHz^{-1}$.

Thus, although the precise character and geometrical orientations of anisotropy in the various regions of the heart are not known with certainty, these simulations do suggest that much of the artifact in reconstructions of the slope of attenuation in dog hearts is due to anisotropy. Specifically, the negative reconstruction values in the left ventricular cavity, underestimation of the slope of attenuation of the papillary muscles, and overestimation of the slope in normal left ventricular myocardium and infarct appear to be consequences of the anisotropy of the ultrasonic attenuation within the walls of the ventricle.

III. Discussion

Methods for ultrasonic imaging frequently include an implicit assumption that the medium is isotropic. To achieve quantitative ultrasonic images in the presence of anisotropy one would have to isolate a component of the parameter to be imaged, such as α_o, β, or ψ, for each point in the region to be imaged. Methods to accomplish this have not been developed. The effects of anisotropy upon tomography have been addressed for the case of vector anisotropy present in time-of-flight measurements in a moving fluid [28] and in zeugmatography [29]. Although successful reconstructions were demonstrated in both cases for special geometries, general methods for reconstructions in the presence of vector anisotropy apparently are not available. Furthermore, vector anisotropy appears to differ fundamentally from that exhibited by ultrasonic attenuation and scattering. The vector-anisotropic measurement consists of an isotropic component, and an anisotropic component which is either positive or negative depending upon the relationship between the wave vector and the anisotropy vector. In terms of the model described here, this amounts to relaxing the constraint $C(\theta) \geq 0$, with the result that the anisotropic components along some paths can cancel. The intrinsic anisotropy modeled here is strictly positive and additive, and no comparable cancellation is possible.

The problem of separating the isotropic and anisotropic components for tomographic imaging is quite challenging. Each projection measurement represents an accumulation of isotropic quantities viewed systematically in angle and anisotropic quantities viewed over a mixture of angles relative to the anisotropy axes. Thus the collection of projection measurements does not appear to contain enough information to resolve anisotropy without a priori information. For example, the projections of the annulus with tangentially directed anisotropy are indistinguishable from those of the equivalent isotropic object to which they reconstruct. A general solution accounting for anisotropy may require additional independent measurements beyond the usual tomographic projections.

Additional features of the issue of anisotropy in reconstructive tomography emerge when considerations are generalized to three dimensions. Anisotropy axes can be expected to lie in a variety of directions, not necessarily parallel to the plane being imaged. As discussed in the Appendix, the anisotropy magnitude β is scaled by $\sin^2 \phi$ where ϕ is the angle between the normal to the image plane and the anisotropy axis. One might speculate whether projections carried out in three-dimensions might contain more information which is useful in resolving anisotropy-related ambiguity than projections confined to a plane in two dimensions.

Up to this point, we have limited our discussions to transmission imaging. We now consider briefly the issue of anisotropy in imaging carried out using reflected ultrasound. If random non-uniformities and anisotropy of the acoustic velocity are sufficiently small, reflection measurements may aid in the separation of isotropic and anisotropic components. Con-

sider the highly idealized case in which the amplitude of the received signal at any particular instant in time is determined primarily by the ultrasonic parameter of interest at a specific spatial position. Since the direction of wave propagation at that spatial position is known, comparing the measurements from that point in space for the various angles of view yields a measure of the angular dependence of the parameter, at least over the range of view angle available. In actual measurements many features complicate this simplistic analysis of reflection imaging in anisotropic media. The attenuation of intervening tissue and its anisotropy introduce a complication which is analogous to the projection measurements of tomography. Random variations in acoustic velocity result in unknown path and beam distortions. The three-dimensional orientation of the intrinsic anisotropy axes further complicates the issue. Nevertheless, reflection measurements may permit at least a partial reduction in the limitations imposed upon quantitative imaging by anisotropy.

Methods of imaging in anisotropic media could make use of multiple images to display the separate components of anisotropic parameters, provided they are separable. For example, one image could be based on the spatial variation of the isotropic component of the index (α_o). Another image could be made from spatial variation of the anisotropy magnitude (β). Indeed, the anisotropy magnitude might prove to be a useful parameter for ultrasonic tissue characterization if it can be related to specific pathologies. Anisotropy-related indices might also play a useful role in imaging for non-destructive evaluation of materials. Thus efforts to characterize systematically the angular dependence of the various ultrasonic parameters would be a valuable component in the ongoing task of tissue and materials characterization.

In summary, the effects of anisotropy on transmission tomographic reconstruction were demonstrated analytically and by simulation. In previous studies of excised dog hearts [6] significant differences were observed between values of the slope of attenuation reconstructed tomographically and values obtained from independent measurements [14,26,27]. In contrast, in the present study reconstructions of a simulated anisotropic heart show good agreement with reconstructions of actual heart. Thus, the differences between tomographic and independent measurements of the slope appear to result from anisotropy. Furthermore, these differences appear to be substantially larger than those due to refraction alone. Anisotropy in ultrasonic scattering, reflection coefficients, speed-of-sound, and attenuation appears to have the potential for corrupting the results of quantitative imaging in reflection as well as transmission measurements. Although anisotropy represents a challenge to the design of quantitative imaging systems, it may also offer the potential for novel methods of tissue and materials characterization.

Appendix

Anisotropic Ensemble Confined to a Plane

A specimen of tissue, such as myocardium, may be comprised of a series of layers with the fibers of each layer oriented in a particular direction [15,16]. We model an isolated region of specimen as a superposition of anisotropic media. Assume the region contains multiple anisotropy axes, and suppose all axes are parallel to a plane in space with orientation angles ϕ_{a_i} $i = 1,2,\ldots,N$ in that plane. We express this in a spherical coordinate system where the common plane is situated at angle θ_a, and the ϕ_{a_i} are angles with respect to the Z axis (refer to Fig. A1). Let the directions of propagation be confined parallel to the x-y plane.

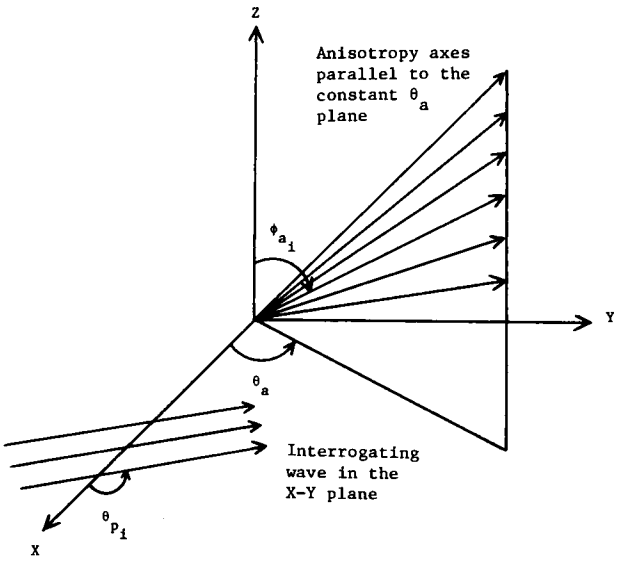

Fig. A1. This diagram illustrates the geometry of an ensemble of anisotropic media lying parallel to a plane, and the interrogating acoustic wave.

If ϕ_p corresponds to the propagation vector, then $\phi_p = \pi/2$, and θ_{p_i} describe the directions of propagation.

The unit vectors parallel to the anisotropy axes are

$$\vec{r}_{a_i} = \hat{i} \cos \theta_a \sin \phi_{a_i} + \hat{j} \sin \theta_a \sin \phi_{a_i} + \hat{k} \cos \phi_{a_i} \tag{A1}$$

where we note that θ_a is constant for all anisotropy axes. The unit vector parallel to the wave propagation direction is

$$\vec{r}_{p_j} = \hat{i} \cos \theta_{p_j} \sin \phi_p + \hat{j} \sin \theta_{p_j} \sin \phi_p + \hat{k} \cos \phi_p \tag{A2}$$

where $\phi_p = \pi/2$ for all waves considered here. Then the angle between wave vector j and anisotropy axis i is

$$\cos \theta_d = \vec{r}_{p_j} \cdot \vec{r}_{a_i} \tag{A3}$$

$$\cos \theta_d = \sin \phi_{a_i} \cos(\theta_a - \theta_{p_j}). \tag{A4}$$

The sinusoidal anisotropic dependence $C(\theta_d)$ is periodic in π, positive, and is defined as

$$C(\theta_d) = \beta \cos^2 \theta_d. \tag{A5}$$

We note also that

$$\cos(2\theta_d) = 2\cos^2\theta_d - 1 \tag{A6}$$

$$= 2\sin^2\phi_{a_i}\cos^2(\theta_a - \theta_{p_j}) - 1 \tag{A7}$$

$$= (2\sin^2\phi_{a_i})(1/2)(\cos[2(\theta_a - \theta_{p_j})] + 1) - 1 \tag{A8}$$

hence,

$$c(\theta_d) = \beta\left[\sin^2\phi_{a_i}\cos[2(\theta_a - \theta_{p_j})] + \sin^2\phi_{a_i}\right]/2 \tag{A9}$$

$$= \beta\sin^2\phi_{a_i}\left[1 + \cos[2(\theta_a - \theta_{p_j})]\right]/2. \tag{A10}$$

When wave j propagates through an object with equal sinusoidal anisotropies at orientations i = 1,2,...,N, each with isotropic component α/N and anisotropy magnitude β, the measurement for the wave j is

$$\alpha_{a_j} = \sum_{i=1}^{N}(\alpha/N)(1 + C(\theta_{d_i})) \tag{A11}$$

$$= (\alpha/N)\sum_{i=1}^{N} 1 + \beta(1 + \cos 2\theta_{d_i})/2 \tag{A12}$$

$$= \alpha\left\{1 + (\beta)(1/N)\left[\sum_{i=1}^{N}\sin^2\phi_{a_i}\right]\cos^2(\theta_a - \theta_{p_j})/2\right\} \tag{A13}$$

$$= \alpha\left\{1 + \beta'\cos^2(\theta_a - \theta_{p_j})/2\right\} \tag{A14}$$

where the anisotropy magnitude apparent in the plane of measurement is

$$\beta' = \beta(1/N)\sum_{i=1}^{N}\sin^2\phi_{a_i} \tag{A15}$$

and the isotropic component of the measurement, α, is constant regardless of the ϕ_{a_i} orientations.

From this brief analysis for measurements in a plane, we conclude: a) If an object, such as the section of left ventricle discussed above, can be modeled as a superposition of anisotropic media whose anisotropy axes are parallel to a plane in space, then the ensemble will exhibit

an anisotropic angular variation whose functional dependence is identical to that of the constituent media, but whose anisotropy magnitude β' is bounded by $o \leq \beta' \leq \beta$ where β is the anisotropy magnitude exhibited by the individual components of the media.

b) Application of the $M_o(\theta)$ zero-order moment to the object modeled above will yield the correct angular dependence function but with an anisotropy magnitude β' which serves as a lower bound for the actual anisotropy exhibited by the individual components of the media in three dimensions. Thus in the case of the rectangular sample of left ventricle, the $M_o(\theta)$ measurement of 2.6 to 1 cited in the text may only be a lower bound because the muscle fibers are not strictly parallel to the plane imaged [15,16].

Acknowledgement

The authors wish to thank Jack G. Mottley for his contributions to this research, Pranoat Suntharothok-Priesmeyer who was responsible for preparation of illustrations, and Polly Raith for preparation of the manuscript.

References

[1] Hueter, T. F., Messung der ultraschallabsorption in tierischen geweben und ihre abhängigkeit von der frequenz, *Die Naturewissenschaft 9*, 285-287 (1948).

[2] Wild, J. J., Reid, J. M., The effects of biological tissue on 15-mc pulsed ultrasound, *J. Acoust. Soc. Amer. 25*, 270-280 (1953).

[3] Goldman, D. E. and Richards, J. R., Measurement of high-frequency sound velocity in mammalian soft tissues, *J. Acoust. Soc. Amer. 26*, 981-983 (1954).

[4] Dussik, K. T., Fritch, D. J., Kyriazidov, M., and Sear, R. S., Measurements of articular tissues with ultrasound, *Amer. J. Physiol. Med. 37*, 160-165 (1958).

[5] Nassiri, D. K., Nicholas, D., and Hill, C. R., Attenuation of ultrasound in skeletal muscle, *Ultrasonics 17*, 230-232 (1979).

[6] Klepper, J. R., Brandenburger, G. H., Mimbs, J. W., Sobel, B. E., and Miller, J. G., Application of phase insensitive detection and frequency dependent measurements to computed ultrasonic attenuation tomography, *IEEE Trans. Biomed. Engineer. BNE-28*, 62-83 (1981).

[7] Klepper, J. R., Brandenburger, G. H., Busse, L. J., and Miller, J. G., Phase Cancellation, Reflection, and Refraction Effects in Quantitative Ultrasonic Attenuation Tomography, in *1977 IEEE Ultrasonics Symposium Proceedings*, pp. 182-188, (IEEE Cat. No. 77CH 1264-1 SU).

[8] Miller, J. G., Klepper, J. R., Brandenburger, G. H., Busse, L. J., O'Donnell, M., and Mimbs, J. W., Reconstructive Tomography Based on Ultrasonic Attenuation, in *Computer Aided Tomography and Ultrasonics in Medicine*, J. Raviv, ed., pp. 151-164 (North Holland, Amsterdam, 1979).

[9] Kak, A. C. and Dines, K. A., Signal processing of broadband pulsed ultrasound: measurement of attenuation of soft biological tissue, *IEEE Trans. Biomed. Engineer. BME-25*, 321-344 (1978).

[10] Dines, K. A., and Kak, A. C., Ultrasonic attenuation tomography of soft tissues, *Ultrasonic Imaging 1*, 16-33 (1979).

[11] Kuc, R., Schwartz, L., and Von Micsky, L., Parametric Estimation of the Acoustic Attenuation Coefficient Slope for Soft Tissue, in *1976 IEEE Ultrasonics Symposium Proceedings*, pp. 44-77, (IEEE Cat. No. 76CH 0994-4 SU).

[12] Busse, L. J., Miller, J. G., Yuhas, D. E., Mimbs, J. W., Weiss, A. N., and Sobel, B. E., Phase Cancellation Effects: A Source of Attenuation Artifact Eliminated by a CdS Acoustoelectric Receiver, in *Ultrasound in Medicine*, 3b, D. White, ed., pp. 1519-1535 (Plenum Press, New York, NY, 1977).

[13] Heyman, J. S., Phase insensitive acoustoelectric transducer, *J. Acoust. Soc. Amer. 64*, 243-249 (1978).

[14] O'Donnell, M., Mimbs, J. W., Sobel, B. E., Miller, J. G., Ultrasonic Attenuation in Normal and Ischemic Myocardium, in *Ultrasonic Tissue Characterization II*, M. Linzer, ed., National Bureau of Standards Spec. Publ. 525, pp. 63-71 (U. S. Government Printing Office, Washington DC, 1979).

[15] Streeter, D. D., Jr., Gross Morphology and Fiber Geometry of the Heart, in *Handbook of Physiology*, R. M. Berne, ed., Vol. 1, Sec. 2, pp. 61-112, (American Physiological Society, MD, 1979).

[16] Streeter, D. D., Jr., Spotnitz, H. M., Patel, D. P., Ross, J., Jr., and Sonnenblick, E. H., Fibre orientation in the canine left ventricle during diastole and systole, *Circulation Research 24*, 339-347 (1969).

[17] Dines, K. A. and Kak, A. C., Ultrasonic attenuation tomography of soft tissues, *Ultrasonic Imaging 1*, 16-33 (1979).

[18] Dick, D. E., Carson, P. L., Bayly, E. J., Oughton, T. V., Kubitscheck, J. E., and Kitson, F. L., Technical Evaluation of an Ultrasound CT Scanner, in *1977 IEEE Ultrasonics Symposium Proceedings*, pp. 176-181, (IEEE Cat. No. 77CH 1264-1 SU).

[19] Carson, P. L., Oughton, T. V., Dick, D. E., Kubitscheck, J. E., Scherzinger, A. L., Kitson, F. L., Johnson, M. L., Lambert, P. A., and Moore, G., Preliminary Characterization of Breast Tissue In Vitro with Ultrasound Computed Tomography of Attenuation, presented at the 3rd International Symposium on Ultrasonic Imaging and Tissue Characterization, National Bureau of Standards, Gaithersburg, MD, June, 1978.

[20] Greenleaf, J. F., Johnson, S. A., Lee, S. L., Herman, G. T., and Wood, E. H., Algebraic Reconstruction of Spatial Distributions of Acoustic Absorption Within Tissue from their Two-Dimensional Acoustic Projections, in *Acoustical Holography*, 5, P. W. Green, ed., pp. 591-603 (Plenum Press, New York, NY, 1974).

[21] Greenleaf, J. F. and Johnson, S. A., Algebraic Reconstruction of Spatial Distributors of Refractive Index and Attenuation in Tissues from Time-of-Flight and Amplitude Profiles, in *Ultrasonic Tissue Characterization*, M. Linzer, ed., National Bureau of Standards Spec. Publ. 453, pp. 109-119, (U. S. Government Printing Office, Washington, DC, 1976).

[22] Greenleaf, J. F., Johnson, S. A., Bahn, R. C., and Rajagopalan, B., Quantitative Cross-Sectional Imaging of Ultrasound Parameters, in *1977 IEEE Ultrasonics Symposium Proceedings*, pp. 989-995, (IEEE Cat. No. 77 CH 1264-1 SU).

[23] Ramachandran, G. N. and Lakshminarayanan, A. V., Three-dimensional reconstruction from radiographs and electron micrographs: application of convolutions instead of Fourier transforms, *Proc. National Acad. Sci. USA* 68, 2236-2249, 1971.

[24] Snyder, D. L. and Cox, J. R., Jr., An Overview of Reconstructive Tomography and Limitations Imposed by a Finite Number of Projections, in *Reconstruction Tomography in Diagnostic Radiology and Nuclear Medicine*, M. M. Ter-Pogossian, et al., eds. (University Park Press, 1977).

[25] Abramowitz, M. and Stegun, I. A., eds. *Handbook of Mathematical Functions*, (Dover, New York, 1970).

[26] O'Donnell, M., Mimbs, J. W., and Miller, J. G., The relationship between collagen and ultrasonic attenuation in myocardial tissue, *J. Acoust. Soc. Amer. 65*, 512-417 (1979).

[27] Mimbs, J. W., O'Donnell, M., Miller, J. G., and Sobel, B. E., Changes in ultrasonic attenuation indicative of early myocardial ischemic injury, *Amer. J. Physiol. 236*, H340 (1979).

[28] Johnson, S. A., Greenleaf, J. F., Hansen, C. R., Samayoa, W. F., Tanaka, M., Lent, A., Christiansen, D. A., and Wooley, R. L., Reconstructing Three Dimensional Fluid Velocity Fields from Acoustical Transmission Measurements, in *Acoustical Holography*, Vol. 7, L. Kessler, ed., pp. 307-326 (Plenum Press, New York, NY, 1977).

[29] Kramer, D. M. and Lauterbur, P. C., On the problem of reconstructing images of non-scalar parameters, application to vector fields, *IEEE Trans. Nuclear Science NS-26*, 2674-2677 (1979).